Research paper

Experimental verification of Hill's model for wood

Jan Pełczyński[1]

Abstract: Structural elements made of wood, are finding more and more applications in construction. They are becoming increasingly popular again due to their ecological nature, as shown by the latest high-rise construction projects. The development of modern wooden structures is forcing designers to look for new solutions in workmanship. New technologies such as glued-laminated timber and cross-laminated timber are currently undergoing many analyses, such as verification for load-bearing capacity, stiffness, fire resistance, acoustics and life cycle assessment. The most popular at present is massive timber. Structures made with this technology consist mainly of cross-laminated and glued-laminated timber elements. Research on cross-laminated timber has mainly focused on its bending and shear strength or modeling approaches to estimate bending strength and failure mechanisms. From the point of view of high-rise construction, aspects of compression behaviors timber elements and their lateral performance are also relevant. In this study, a nonlinear material model based on Hill's anisotropic plasticity potential was calibrated to determine the extent to which it is suitable for simulating simple experimental tests. To this end, experimental compression tests were carried out on wooden specimens at three different angles to the fiber direction. Data from the experiments were collected in parallel using two methods: reading the force and displacement of the machine head; and using the Aramis system to observe the surface of the specimen and determine the displacements using DIC. For comparison with numerical models, both displacement fields and force-displacement curves were averaged against individual samples using proprietary codes written in Python.

Keywords: digital image correlation, finite element method, glued-laminated timber, laboratory tests

---

[1]PhD., Eng., Warsaw University of Technology, Faculty of Civil Engineering, Al. Armii Ludowej 16, 00-637 Warsaw, Poland, e-mail: jan.pelczynski@pw.edu.pl, ORCID: 0000-0002-6983-8480

1. Introduction

Structural elements made of wood have many advantages, from their high load-bearing capacity to element weight ratio to their environmental properties, among which are the ability to store CO_2 or the renewability of the raw material. They are finding more and more applications, as wooden structures are becoming increasingly popular again due to their ecological nature, as shown by recent high-rise construction projects [1]. The development of modern wooden structures is forcing designers to look for new solutions in workmanship. New technologies such as glued-laminated timber and cross-laminated timber are currently undergoing many analyses, such as verification for fire resistance [2] or life cycle assessment [3].

The most popular today is massive wood. Structures made with this technology consist entirely of elements made of glued-laminated timber (GLT) and cross-laminated timber (CLT). GLT consists of layers about 4 cm thick, laid in the same direction, which, when glued together, form elements that are usually used as columns or beams. CLT, on the other hand, is formed by gluing lamellas with alternating perpendicular directions, allowing for panel elements. The research on glued-laminated timber has focused mainly on its bending and shear performance [4] or modeling approaches to estimate the bending strength and failure mechanisms [5]. From a high-rise construction perspective, aspects of compression behaviors of cross-laminated timber and glued-laminated timber columns [6] and its lateral performance [7] are also important.

Another aspect analyzed in the modern literature is the acoustics of solid wood components [8, 9]. On the other hand, from the point of view of experimental modeling of joints and the way they are made, for example publications [10–14] are relevant, among which should be mentioned those dealing with the study of Kirchhoff modulus [15–17], since this is a topic that is still not adequately studied. It is noteworthy that Digital Image Correlation (DIC) can be used during the study of wood, which, combined with numerical modeling, allows a more accurate analysis of the behavior of the structure or its components [18].

In the present study, a nonlinear material model based on Hill's anisotropic plasticity potential was calibrated. The aim of the present paper is to determine the extent to which the material model is suitable for simulating simple experimental tests. In addition, the presented method makes it possible to determine the Kirchhoff modulus, which is a difficulty addressed in many research papers. This is made possible by the use of inverse analysis in determining the material parameters of the model. To this end, experimental compression tests were carried out on wooden specimens at three different angles to the fiber direction. Data from the experiments were collected in parallel using two methods: reading the force and displacement of the machine head; and using the Aramis system to observe the surface of the specimen and determine the displacements using Digital Image Correlation. For comparison with numerical models, both displacement fields and force-displacement curves were averaged against individual samples using original codes written in Python.

2. Laboratory tests

2.1. Test stand and sample preparation

As part of the conducted research, compression experiments were carried out on spruce samples in three directions in relation to the wood fibers. Fig. 1. shows the specimens: (a) for compression testing along the fibers (labeled C00); (b) across the fibers (C90); (c) at an angle 45° to the fibers (C45). The C00 specimens, 360 mm in length, were cut from a 60 mm × 120 mm beam. They were then milled to a width of 42 mm on a center section 157 mm long. C90 specimens, 250 mm long, were cut from a beam with a section of 100 mm × 200 mm. The C45 specimens were cut from a beam with a cross-section of 140 mm × 280 mm in such a way that the resulting pieces were 140 mm × 180 mm × 180 mm. The dimensions of the samples were chosen to best meet the requirements of the standard [19]. The way the samples were cut out is shown in Fig. 2.
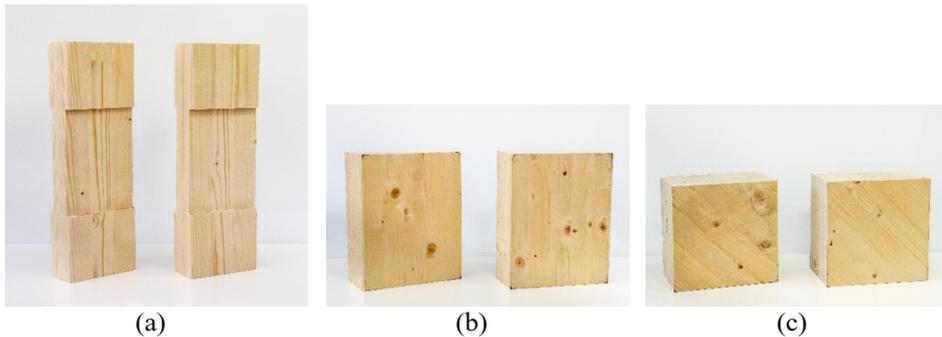
Fig. 1. Samples prepared for testing: (a) compression along the fibers; (b) compression across the fibers; (c) compression at an angle 45° to the fibers
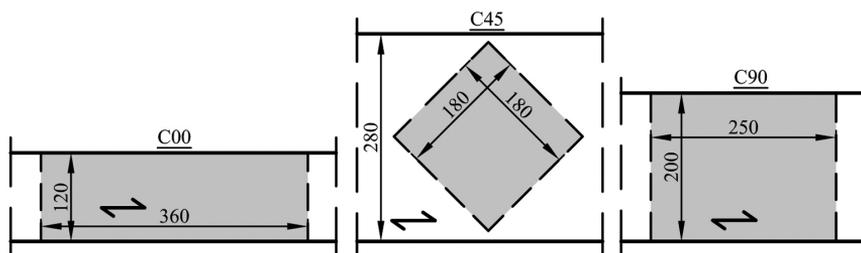
Fig. 2. Cutout direction and dimensions of C00, C45 and C90 samples, in millimeters

A pattern consisting of randomly distributed black points on a white background was applied to each sample, as shown in Fig. 3. In addition, four points defining the corners of the measurement field were marked on them. These points were later used to determine the exact position of the observed pattern relative to the numerical model. The measurement fields had the following dimensions: for C00, 100 mm × 130 mm; for C90, 180 mm × 150 mm; for C45, 140 mm × 140 mm.
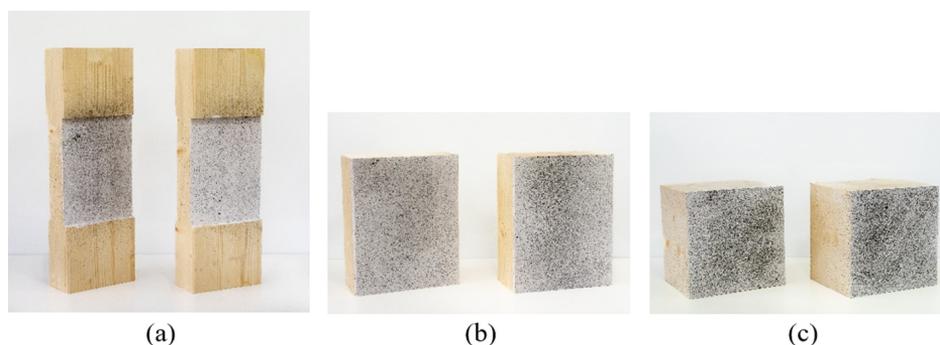
Fig. 3. Samples prepared for testing: (a) compression along the fibers; (b) compression across the fibers;
(c) compression at an angle 45°to the fibers; after applying the pattern for digital image correlation

The tests were carried out in an Instron 8802 machine connected to an Aramis system with software version v6.2.0. Fig. 4 shows a C45 sample prepared for testing. The samples were tested immediately after being taken out of the climate chamber. The specimens were loaded with a constant displacement increment of 2 mm/min.
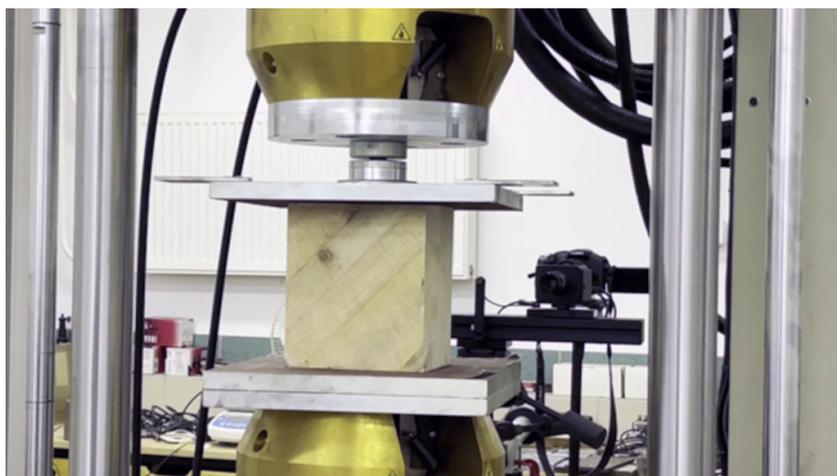
Fig. 4. Test stand with mounted C45 sample. Aramis system camera visible in the background

2.2. Laboratory test results

Displacement fields of the sample surface observed with the Aramis system and force-displacement curves, taken directly from Instron readings, were obtained as test results. Displacement fields were recorded on the entire surface of the sample, falling within the field of view of the cameras. Only a part of the surface, falling within the area of the measurement field, indicated in Fig. 5, was analyzed.
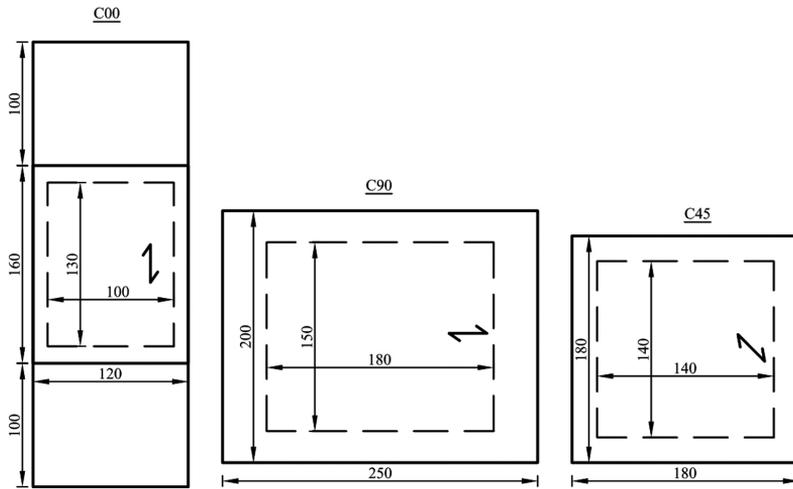
Fig. 5. Location of the measurement field for specimens C00, C90, C45, in millimeters

Figs. 6–8 show the force-displacement curves for C00 (obtained for three samples), C90 (obtained for five samples) and C45 (obtained for three samples), respectively.
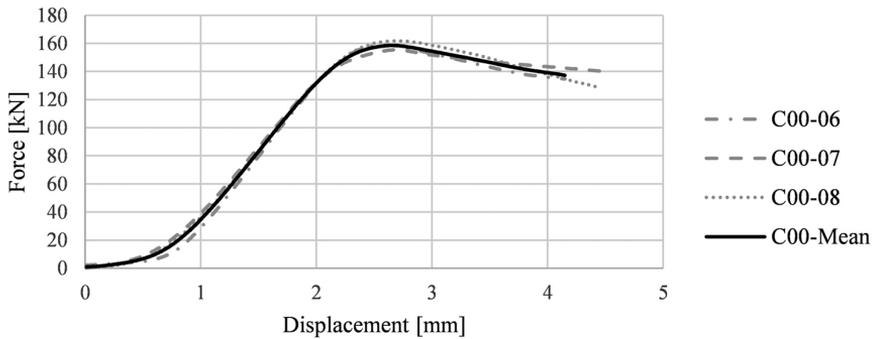
Fig. 6. Force-displacement curves for compression test along fibers, C00
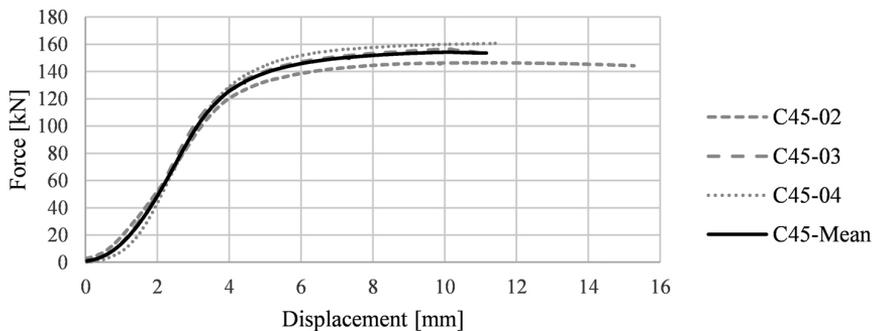
Fig. 7. Force-displacement curves for compression test at angle 45° against fibers, C45
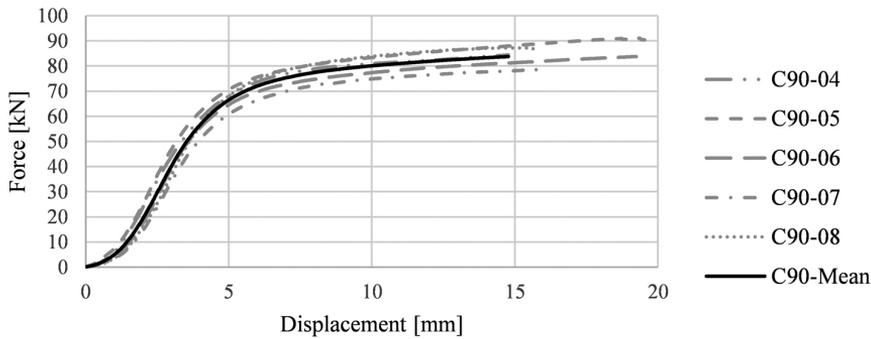
Fig. 8. Force-displacement curves for compression test across fibers, C90

The graphs show the change in the total force applied to the specimen as a function of the displacement imposed on its upper plane. The curvature in the initial phase is due to the settling of the specimen and possible inaccuracies in its manufacture. This is followed by a linear phase, corresponding to the elastic range, which is later replaced by a nonlinear phase, resulting from material failure.

Acting in accordance with the standard [19], the maximum force and strengths corresponding to the tests were determined. Based on the analysis of force-displacement curves, force values were also adopted, determining the linear range. The results are shown in Table 1.

Table 1. Maximum forces and strengths obtained from force-displacement curves

Specimen name	F_{max} [kN]	$F_{lower}^{elastic}$ [kN]	$F_{upper}^{elastic}$ [kN]	f_c* [MPa]	f_c mean* [MPa]	Moisture content [%]
C00-06	158.8			31.0		14.9
C00-07	155.5	48.8	99.2	30.3	31.0	15.8
C00-08	161.9			31.6		15.4
C90-04	83.1			3.0		15.7
C90-05	81.3			3.1		14.6
C90-06	75.1	14.4	33.6	2.9	3.0	15.4
C90-07	74.7			2.8		15.6
C90-08	80.1			3.1		16.7
C45-02	138.6			4.9		16.7
C45-03	145.7	53.7	99.3	5.2	5.2	16.5
C45-04	151.3			5.4		16.3
*For C00 samples it is $f_{c,0}$, for C45 it is $f_{c,45}$, for C90 it is $f_{c,90}$.						

In order to compare with the results of numerical models, the displacement fields obtained from the tests were averaged. This was done in the elastic range. Due to the initial curvature of the graph, the length of the linear range was determined based on [19], but the range was

shifted upward to include only the linear part of the curve. It was assumed that for C00, the elastic range covers 50.3 kN, starting from a load equal to 48.8 kN; for C45, it covers 45.6 kN, starting from a load equal to 53.7 kN; for C90, it covers 19.1 kN, starting from a load equal to 14.4 kN. To average the individual fields, displacement values were exported from the Aramis program, read at points defined by the pattern previously applied to the specimens (see Fig. 2) and the layout of the facets. Then, using the author's Python code and the *scipy* library [20], piecewise linear interpolation of the displacement values was performed. The next step was to define a regular grid of points and read the displacement values at these points. This made it possible to average the displacement values at corresponding sample points with the same coordinates. The averaged fields are shown in Figs. 9–11. What is clearly visible, the
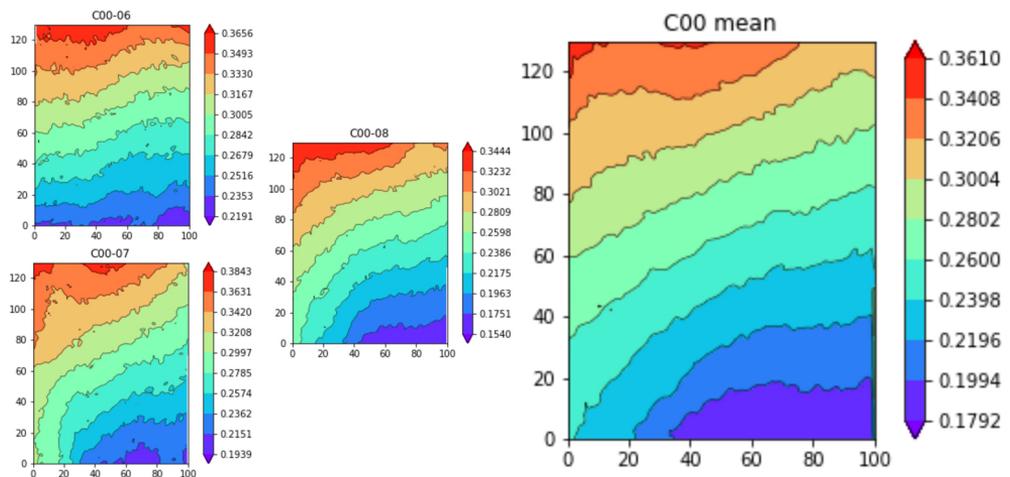
Fig. 9. Fields of resultant displacements [mm] for three C00 specimens for an increment of $\Delta F = 50.3$ kN and the averaged field
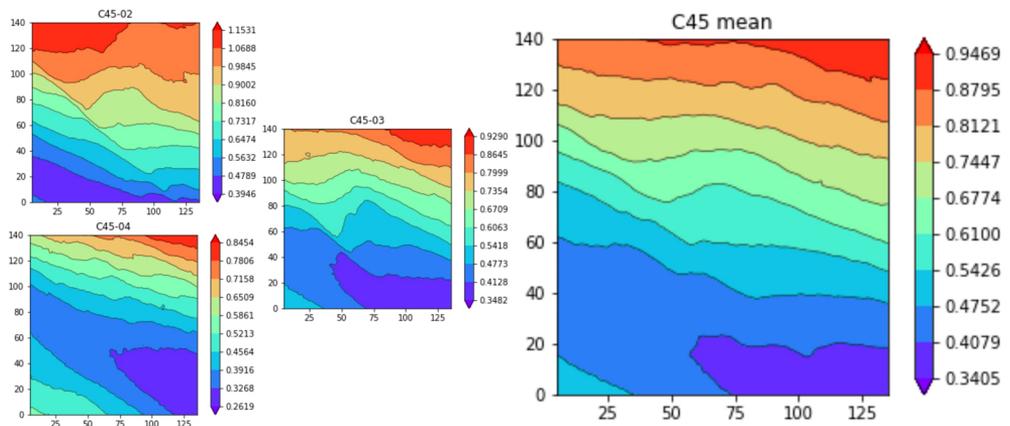
Fig. 10. Fields of resultant displacements [mm] for three C45 specimens for an increment of $\Delta F = 45.6$ kN and the averaged field
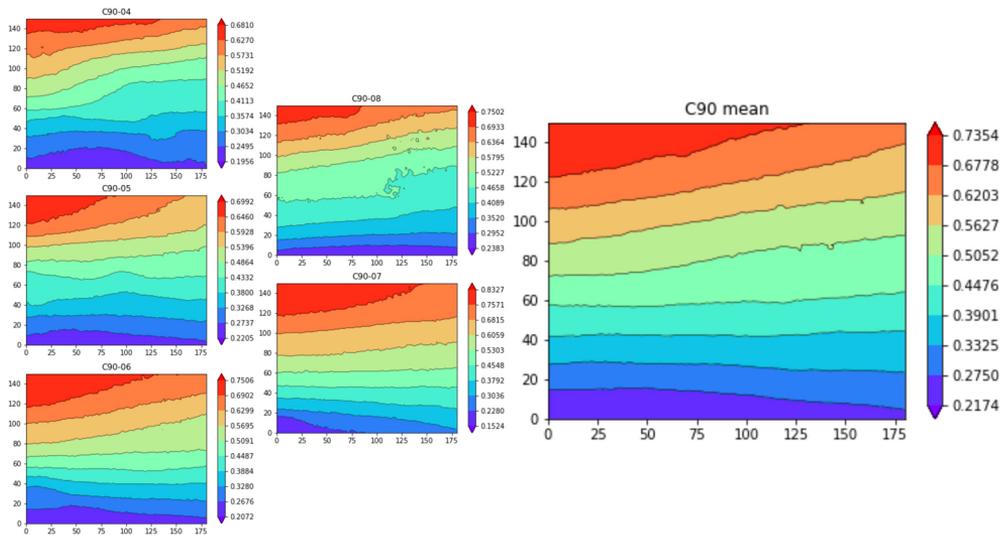
Fig. 11. Fields of resultant displacements [mm] for five C90 specimens for an increment of $\Delta F = 19.1$ kN and averaged field

displacement fields of individual samples differ. According to the author, the differences are mainly due to the inhomogeneity of the samples, the different arrangement of knots and the uneven arrangement of fibers, which is partially visible in Fig. 1.

3. Numerical analysis

3.1. Numerical model

As part of the numerical analysis, three finite element method models were made using Abaqus 2018, corresponding to the three types of compression tests performed earlier. The geometry of each model is shown in Fig. 12.

Each model consisted of three elements: a deformable object simulating a wooden specimen and two rigid plates. Between the wooden element and the plates, contact normal to the surface of the plate and friction with a coefficient equal to 0.5 were assumed. A vertical displacement imposed at the center of the upper plate was assumed as the load. The lower slab was fixed with zero boundary conditions. 3D stress 8-node brick elements with linear shape functions C3D8R with edge lengths of about 12 mm were used. The model used an orthotropic material model. In the first stage, an elastic material was analyzed, characterized by nine independent parameters [21]: three Young's moduli (E_1, E_2, E_3), three Poisson's coefficients (v_{12}, v_{13}, v_{23}) and three Kirchhoff's moduli (G_{12}, G_{13}, G_{23}). Since the present paper did not distinguish between tangential and radial directions, the calculations assumed that Young's moduli in
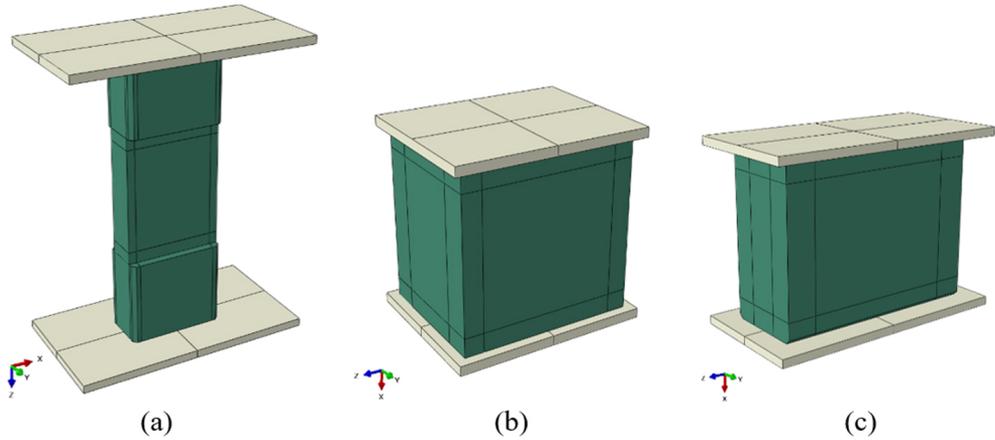
Fig. 12. Numerical models of (a) compression along the fibers; (b) compression across the fibers; (c) compression at an angle 45° to the fibers

transverse directions are equal to each other $E_2 = E_3$ and that $\nu_{12} = \nu_{13} = \nu_{23} = \nu$ and $G_{12} = G_{13} = G_{23} = G$.

In the second step of the analysis, plasticity was added in the form of Hill anisotropic plasticity potential [22], defined as

$$(3.1) \quad f(\boldsymbol{\sigma}) = \sqrt{F(\sigma_{22} - \sigma_{33})^2 + G(\sigma_{33} - \sigma_{11})^2 + H(\sigma_{11} - \sigma_{22})^2 + 2L\sigma_{23}^2 + 2M\sigma_{31}^2 + 2N\sigma_{12}^2}$$

where the constants F, G, H, L, M, N are defined as

$$(3.2) \quad \begin{aligned} F &= \frac{1}{2}\left(\frac{1}{R_{22}^2} + \frac{1}{R_{33}^2} - \frac{1}{R_{11}^2}\right), \quad G = \frac{1}{2}\left(\frac{1}{R_{33}^2} + \frac{1}{R_{11}^2} - \frac{1}{R_{22}^2}\right), \\ H &= \frac{1}{2}\left(\frac{1}{R_{11}^2} + \frac{1}{R_{22}^2} - \frac{1}{R_{33}^2}\right), \quad L = \frac{3}{2R_{23}^2}, \quad M = \frac{3}{2R_{13}^2}, \quad N = \frac{3}{2R_{12}^2} \end{aligned}$$

whereas the coefficients R_{ij} are anisotropic yield stress ratios, defined as follows:

$$(3.3) \quad R_{11} = \frac{f_{11}}{f_0}, \quad R_{22} = \frac{f_{22}}{f_0}, \quad R_{33} = \frac{f_{33}}{f_0}, \quad R_{12} = \sqrt{3}\frac{f_{12}}{f_0}, \quad R_{13} = \sqrt{3}\frac{f_{13}}{f_0}, \quad R_{23} = \sqrt{3}\frac{f_{23}}{f_0}$$

where f_0 is the reference strength. In this case, calculations were carried out assuming geometric nonlinearities.

3.2. Research methodology and results

In the first step of the analysis, the material parameters of the numerical model were calibrated with the results of experimental tests in the elastic range. For this purpose, a norm was defined, allowing to evaluate the quality of the displacement field obtained from the model in relation to the test result. The norm is expressed by the formula

$$(3.4) \qquad \delta = \frac{\sum_{i=1}^{n} \sqrt{(x_i^{\text{num}} - x_i^{\text{lab}})^2 + (y_i^{\text{num}} - y_i^{\text{lab}})^2}}{n}$$

in which n is the number of points, x_i^{num}, y_i^{num} are the horizontal and vertical displacements of the i-th point obtained from the numerical model, and x_i^{lab}, y_i^{lab} are the analogous displacements of the averaged displacement field from laboratory tests. This norm is denoted in mm and can be interpreted as the distance between two displacement fields.

In the first step of the elastic range calibration, the effect of individual material parameters on the behavior of the numerical model was checked. Using Python code, multiple Abaqus input files with different material parameters were generated, based on which Abaqus performed finite element method calculations. As expected, in the C00 model, the Young's modulus along the fibers had the greatest influence on the value of the standard (3.1). The smallest δ between the C00 numerical model and the experiment was obtained for $E_1 = 4139$ MPa, as can be seen in Fig. 13. The analysis showed that the other parameters had no significant effect on the value of the standard. Similarly, a value of $E_2 = 168$ MPa was obtained from the C90 model (see Fig. 14), in which the other parameters also had a negligible effect on the distance δ.
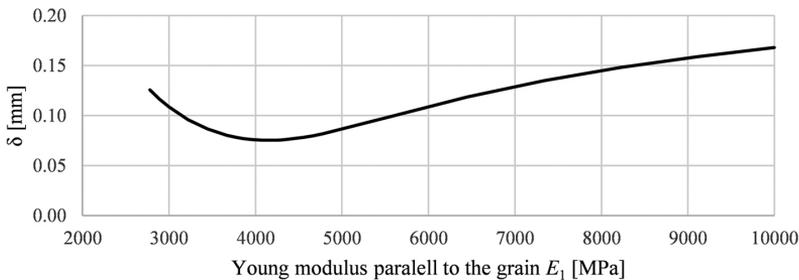
Fig. 13. Dependence of the distance δ between the numerical model C00 and the experiment on the modulus of E_1, assuming $E_2 = 165$ MPa, $G = 510$ MPa, $\nu = 0.35$
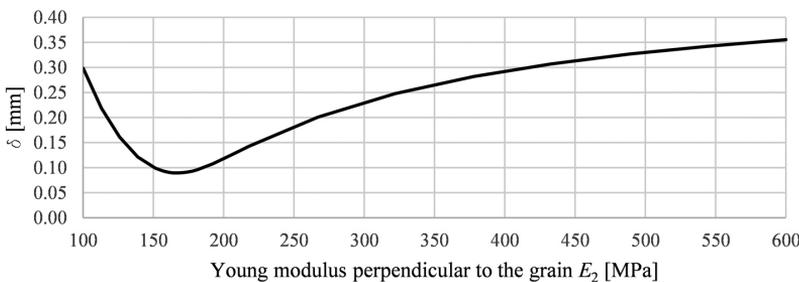
Fig. 14. Dependence of the distance δ between the numerical model C90 and the experiment on the modulus of E_2, assuming $E_1 = 3667$ MPa, $G = 510$ MPa, $\nu = 0.35$

Then, based on the $E_1 E_2$ parameters obtained from previous models, the G parameter in the C45 model was calibrated. The smallest distance δ between the C45 numerical model and the experiment was obtained for $G = 123$ MPa, as shown in Fig. 15.
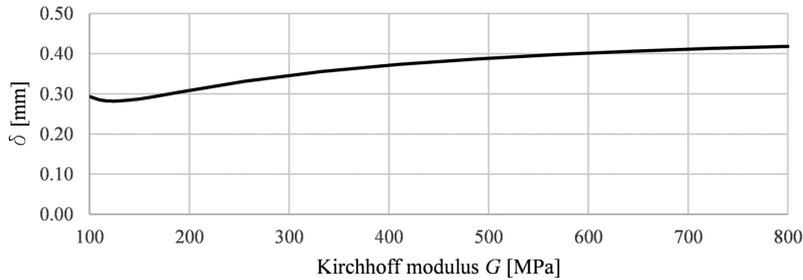
Fig. 15. Dependence of the distance δ between the numerical model C45 and the experiment on the modulus of G, assuming $E_1 = 4139$ MPa, $E_2 = 168$ MPa, $\nu = 0.35$

In order to correctly represent the plastic behavior of the model, the compressive strength values of each specimen were determined based on the $F_{\max}$ value given in Table 1. For C00 specimens, $f_{c,0} = 31.0$ MPa was obtained, for C45 $f_{c,45} = 5.2$ MPa, and for C90 $f_{c,90} = 3.0$ MPa. These values were used to determine the coefficients (3.2) of the elastic potential as follows. According to [23], reducing the task to a plane state of stress and assuming a uniaxial state of stress corresponding to compression at an angle α to the direction of the fibers, the relationship between the compressive strength in this direction and the value of the potential (3.1) can be written as

$$(3.5) \qquad R_c(\alpha) = \frac{1}{\sqrt{F \sin^4(\alpha) + G \cos^4(\alpha) + H \cos^4(2\alpha) + 2N \sin^2(\alpha) \cos^2(\alpha)}}$$

in order to determine the parameters F, G, H, N the task of minimizing the function $C(F, G, H, N)$ given by the formula

$$(3.6) \qquad C(F, G, H, N) = (R_c(0) - f_{c,0})^2 + (R_c(45) - f_{c,45})^2 + (R_c(90) - f_{c,90})^2$$

with respect to these coefficients was performed. The following values were obtained

$$(3.7) \qquad F = 0.11030, \quad G = 0.00023, \quad H = 0.00081, \quad N = 0.01870$$

which leads to the following values of coefficients R

$$(3.8) \qquad R_{11} = 31.0, \quad R_{22} = R_{33} = 3.0, \quad R_{13} = R_{23} = R_{12} = 8.96$$

The obtained values of the coefficients were implemented into the nonlinear material model in the Abaqus program, assuming a reference strength of 1 MPa. The force-displacement curves obtained for each model are presented in Fig. 16–18.

As is visible in the curves shown, the numerical models corresponding to samples C00 and C90 show elastic-perfectly plastic behavior. In the case of C90, there is a slight strengthening after the beginning of nonlinearity. In the C45 sample model, the force-displacement curve obtained numerically shows a curvature similar to the averaged curve obtained from tests. All three models show a very good representation of the specimen's stiffness in the elastic range.
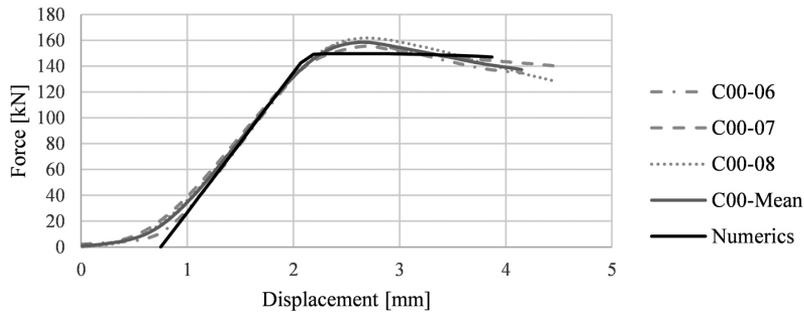
Fig. 16. Force-displacement curves for compression test along fibers, C00, with numerical curve added
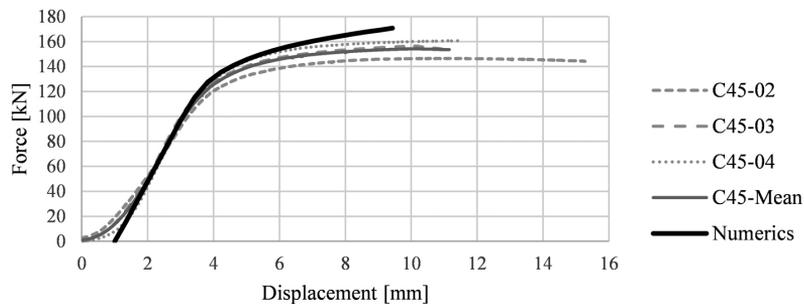
Fig. 17. Force-displacement curves for compression test at angle 45° against fibers, C45, with numerical curve added
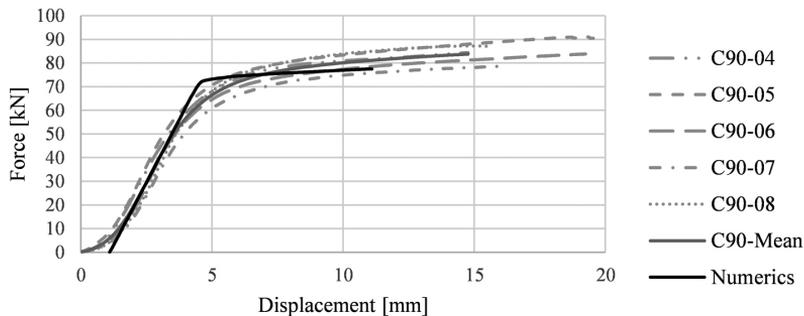
Fig. 18. Force-displacement curves for compression test across fibers, C90, with numerical curve added

Analyzing the curves, it can be concluded that the C00 and C45 test models predict well the beginning of the nonlinear behavior of the material, while in the C90 test model, yielding begins later than in the experimental test. The maximum forces, read according to the procedure in standard [19], are as follows: for model C00 the force F_{max} = 149.7 kN, C45 the force F_{max} = 158.2 kN, C90 the force F_{max} = 75.0 kN. These are close to the values held from experience, equal to 158.7 kN, 145.2 kN, and 74.4 kN, respectively.

4. Summary and conclusions

The preparation of numerical models and their calibration requires a series of experimental tests, which are necessary to determine the calibration parameters. In order to determine them, experimental compression tests were carried out on wooden specimens at three different angles to the fiber direction. Data from the experiments were collected in parallel using two methods: the Aramis system for observing the surface of the specimen and determining displacements using digital image correlation; and reading the force and displacement of the test machine head. The first set of data was used as the basis for determining the elastic parameters of the material, while the second was used primarily for nonlinear range analysis. It is important that the proposed method allows the determination of Kirchhoff's modulus, which is a difficulty addressed in many research papers.

Taking into account the experiments carried out and the results of numerical modeling, it can be concluded that the developed model reflects the behavior of the samples in the linear range very well. In the nonlinear range, the maximum forces obtained from the numbers are close to those determined from the experimental tests, but the force-displacement curves do not perfectly reflect the shape of the curves from the tests.

In order to improve the results obtained and increase the accuracy of the numerical models, the present author plans to expand the experimental database by repeating the tests performed on a more numerous sample. In addition, the numerical models can gain by introducing "softened contact" to reflect the nonlinear behavior of the sample in the first loading phase, corresponding to the initial settling of the sample. This approach takes into account the functional stress increment at the interface of the elements at which contact occurs, as the distance between them changes, unlike "hard contact", in which for zero distance between elements there is an infinite increase in stresses. Another aspect to be tested will be the verification of the results using a more elaborate formulation of the plastic potential, for example by implementing mutlisurface plasticity [24–26].

References

[1] L. Tupenaite, V. Zilenaite, L. Kanapeckiene, T. Gecys, and I. Geipele, "Sustainability assessment of modern high-rise timber buildings", *Sustainability*, vol. 13, no. 16, art. no. 8719, 2021, doi: 10.3390/su13168719.

[2] D. Barber, "Fire safety of mass timber buildings with clt in usa", *Wood and Fiber Science*, vol. 50, pp. 83–95, 2018, doi: 10.22382/wfs-2018-042.

[3] Z. Duan, Q. Huang, and Q. Zhang, "Life cycle assessment of mass timber construction: A review", *Building and Environment,* vol. 221, art. no. 109320, 2022, doi: 10.1016/j.buildenv.2022.109320.

[4] H. Li, L. Wang, Y. Wei, B. J. Wang, and H. Jin, "Bending and shear performance of cross-laminated timber and glued-laminated timber beams: A comparative investigation", *Journal of Building Engineering*, vol. 45, art. no. 103477, 2022, doi: 10.1016/j.jobe.2021.103477.

[5] C. Vida, M. Lukacevic, J. Eberhardsteiner, and J. Füssl, "Modeling approach to estimate the bending strength and failure mechanisms of glued laminated timber beams", *Engineering Structures*, vol. 255, art. no. 113862, 2022, doi: 10.1016/j.engstruct.2022.113862.

[6] P. Wei, B. J. Wang, H. Li, L. Wang, S. Peng, and L. Zhang, "A comparative study of compression behaviors of cross-laminated timber and glued-laminated timber columns", *Construction and Building Materials*, vol. 222, pp. 86–95, 2019, doi: 10.1016/j.conbuildmat.2019.06.139.

[7] J. Xue, G. Ren, L. Qi, C. Wu, and Z. Yuan, "Experimental study on lateral performance of glued-laminated timber frame infilled with cross-laminated timber shear walls", *Engineering Structures*, vol. 239, art. no. 112354, 2021, doi: 10.1016/j.engstruct.2021.112354.

[8] C. Fenemore, "Acoustics of cross-laminated timber structures", Ph.D. thesis, The University of Auckland, 2023.

[9] V. Nasir, S. Ayanleye, S. Kazemirad, F. Sassani, and S. Adamopoulos, "Acoustic emission monitoring of wood materials and timber structures: A critical review", *Construction and Building Materials*, vol. 350, art. no. 128877, 2022, doi: 10.1016/j.conbuildmat.2022.128877.

[10] M. Braun and B. Kromoser, "The influence of inaccuracies in the production process on the load-bearing behaviour of timber step joints", *Construction and Building Materials*, vol. 330, art. no. 127285, 2022, doi: 10.1016/j.conbuildmat.2022.127285.

[11] M. Braun, M. Pantscharowitsch, and B. Kromoser, "Experimental investigations on the load-bearing behaviour of traditional and newly developed step joints for timber structures", *Construction and Building Materials*, vol. 323, art. no. 126557, 2022, doi: 10.1016/j.conbuildmat.2022.126557.

[12] M. Braun, J. Pełczyński, A. Al Sabouni-Zawadzka, and B. Kromoser, "Calibration and validation of a linear-elastic numerical model for timber step joints based on the results of experimental investigations", *Materials*, vol. 15, no. 5, art. no. 1639, 2022, doi: 10.3390/ma15051639.

[13] B. Kromoser, M. Braun, and M. Ortner, "Construction of all-wood trusses with plywood nodes and wooden pegs: a strategy towards resource-efficient timber construction", *Applied Sciences*, vol. 11, no. 6, art. no. 2568, 2021, doi: 10.3390/app11062568.

[14] M. Pantscharowitsch, M. Braun, and B. Kromoser, "Experimental investigations on the load-bearing behaviour of robot-manufactured timber-timber joints", presented at World Conference on Timber Engineering, Chile, 2021.

[15] S. Berg, J. Turesson, M. Ekevad, and A. Björnfot, "In-plane shear modulus of cross-laminated timber by diagonal compression test", *BioResources*, vol. 14, no. 3, pp. 5559–5572, 2019, doi: 10.15376/biores.14.3.5559-5572.

[16] J. Turesson, A. Björnfot, S. Berg, M. Ekevad, and R. Tomasi, "Picture frame and diagonal compression testing of cross-laminated timber", *Materials and Structures*, vol. 52, pp. 1–12, 2019, doi: 10.1617/s11527-019-1372-7.

[17] K. Ostapska and K. A. Malo, "New approach to testing shear in wood on structural scale", *International Journal of Solids and Structures*, vol. 212, pp. 46–60, 2021, doi: 10.1016/j.ijsolstr.2020.11.022.

[18] C. Timbolmas, F. J. Rescalvo, M. Portela, and R. Bravo, "Analysis of poplar timber finger joints by means of digital image correlation (dic) and finite element simulation subjected to tension loading", *European Journal of Wood and Wood Products*, vol. 80, no. 3, pp. 555–567, 2022, doi: 10.1007/s00107-022-01806-6.

[19] EN 408:2010+A1:2012 Timber structures – Structural timber and glued laminated timber – Determination of some physical and mechanical properties. CEN, 2012.

[20] "SciPy documentation, Version: 1.11.4". [Online]. Available: https://docs.scipy.org/doc/scipy/index.html. [Accessed: 27. Nov. 2023].

[21] P. Obara, "Verification of orthotropic model of wood", *Archives of Civil Engineering*, vol. 64, no. 3, pp. 31–44, 2018.

[22] Abaqus Version 6.13. Simulia. Abaqus: Providence, RI, USA, 2013.

[23] K. A. Malo, O. S. Hopperstad, and O. G. Lademo, "Calibration of anisotropic yield criteria using uniaxial tension tests and bending tests", *Journal of Materials Processing Technology,* vol. 80-81, pp. 538–544, 1998, doi: 10.1016/S0924-0136(98)00202-7.

[24] S. Pech, M. Lukacevic, and J. Füssl, "A robust multisurface return-mapping algorithm and its implementation in Abaqus", *Finite Elements in Analysis and Design*, vol. 190, art. no. 103531, 2021, doi: 10.1016/j.finel.2021.103531.

[25] M. Lukacevic, W. Lederer, and J. Füssl, "A microstructure-based multisurface failure criterion for the description of brittle and ductile failure mechanisms of clear-wood", *Engineering Fracture Mechanics*, vol. 176, pp. 83–99, 2017, doi: 10.1016/j.engfracmech.2017.02.020.

[26] M. Lukacevic, J. Füssl, and R. Lampert, "Failure mechanisms of clear wood identified at wood cell level by an approach based on the extended finite element method", *Engineering Fracture Mechanics*, vol. 144, pp. 158–175, 2015, doi: 10.1016/j.engfracmech.2015.06.066.

Eksperymentalna weryfikacja modelu Hilla dla drewna

Słowa kluczowe: cyfrowa korelacja obrazu, metoda elementów skończonych, drewno klejone warstwowo, testy laboratoryjne

Streszczenie:

Elementy konstrukcyjne wykonane z drewna znajdują coraz więcej zastosowań w budownictwie. Stają się one coraz bardziej popularne ze względu na swój ekologiczny charakter, czego dowodem są najnowsze projekty wieżowców. Rozwój nowoczesnych konstrukcji drewnianych zmusza projektantów do poszukiwania nowych rozwiązań w wykonawstwie. Nowe technologie, takie jak drewno klejone warstwowo i drewno klejone krzyżowo, są obecnie poddawane wielu analizom, takim jak weryfikacja pod kątem nośności, sztywności, odporności ogniowej, akustyki i oceny cyklu życia. Najpopularniejsze obecnie jest drewno masywne. Konstrukcje wykonane w tej technologii składają się głównie z elementów z drewna klejonego krzyżowo i warstwowo. Badania nad drewnem klejonym krzyżowo koncentrowały się głównie na jego wytrzymałości na zginanie i ścinanie lub podejściach do modelowania w celu oszacowania wytrzymałości na zginanie i mechanizmów uszkodzeń. Z punktu widzenia konstrukcji wieżowców istotne są również aspekty zachowania elementów drewnianych podczas ściskania i ich właściwości boczne. W tym badaniu skalibrowano nieliniowy model materiałowy oparty na anizotropowym potencjale plastyczności Hilla, aby określić, w jakim stopniu nadaje się on do symulacji prostych testów eksperymentalnych. W tym celu przeprowadzono eksperymentalne testy ściskania na drewnianych próbkach pod trzema różnymi kątami w stosunku do kierunku włókien. Dane z eksperymentów były zbierane równolegle przy użyciu dwóch metod: odczytu siły i przemieszczenia głowicy maszyny; oraz przy użyciu systemu Aramis do obserwacji powierzchni próbki i określania przemieszczeń za pomocą DIC. W celu porównania z modelami numerycznymi, zarówno pola przemieszczeń, jak i krzywe siła-przemieszczenie zostały uśrednione dla poszczególnych próbek przy użyciu autorskich kodów napisanych w języku Python.